Chemical Geology 630 (2023) 121444

Contents lists available at ScienceDirect

Chemical Geology

journal homepage: www.elsevier.com/locate/chemgeo

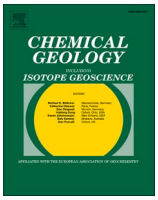

Radiogenic Pb in xenotime trapped in nanoscale inclusions of apatite during fluid alteration

Cilva Joseph [a,b,*], Denis Fougerouse [a,b], Steven M. Reddy [a,b], Hugo K.H. Olierook [a], Tommaso Tacchetto [a,b], Allen Kennedy [d], David W. Saxey [b,d], William D.A. Rickard [b,d], Steven Denyszyn [c], Aaron Dodd [d]

[a] School of Earth and Planetary Sciences, Curtin University, Perth, Australia
[b] Geoscience Atom Probe, John de Laeter Centre, Curtin University, Perth, Australia
[c] Department of Earth Sciences, Memorial University of Newfoundland, Canada
[d] John de Laeter Centre, Curtin University, Perth, Australia

ARTICLE INFO

Editor: Marco Fiorentini

Keywords:
Xenotime
Fluid interaction
Geochronology
Nanoscale
Apatite inclusions

ABSTRACT

This study focuses on the low-temperature mineralogical response of xenotime, a phosphate mineral routinely used as a geochronometer, to fluid-assisted alteration. The studied xenotime grain (z6413) comes from a ~ 1000 Ma pegmatite from the Grenville Province, Canada, and is commonly used as reference material for U—Pb analyses. At the microscale, the grain has a mottled texture, sub-micrometer porosity, and small domains dark in backscattered electron (BSE) images that are characterised by curviplanar, sharp boundaries. The small dark BSE domains are associated with Th-U-rich inclusions and larger porosity (2–3 μm) and are interpreted to result from localised fluid-assisted coupled dissolution-reprecipitation. Sensitive high-resolution ion microprobe (SHRIMP) U—Pb analyses of unaltered and fluid-affected domains yield concordant crystallisation dates, irrespective of the textural domains. The apparently unaltered xenotime domain was characterised at the nanoscale to determine if the grain was affected by fluids beyond the altered domains defined by BSE imaging. Transmission electron microscopy (TEM) imaging results indicate the presence of randomly distributed Ca + Pb nanoscale precipitates. Atom probe tomography (APT) reveals the presence of spherical clusters (4 to 18 nm in size) enriched in radiogenic Pb, Ca, and Si atoms, which, combined with TEM observations, are interpreted as nanoscale inclusions of apatite. In addition to the inclusions, a dislocation enriched in Ca and fluid mobile elements such as Cl, Li, Na, and Mn was imaged from APT data indicating percolating of fluids further than the reaction front. APT $^{206}Pb/^{238}U$ nanogeochronology indicates that the nanoscale inclusions of apatite formed at 863 ± 28 Ma, 100–150 Ma after crystallisation of the host xenotime, with its formation attributed to fluid metasomatism. This study shows that fluid-xenotime reaction caused Pb* to be redistributed at the nanoscale, recording the timing of metasomatism. However, at the scale of SHRIMP analytical spot (10 μm), xenotime is concordant, indicating that Pb was not mobile at the microscale and fluid-altered xenotime can preserve its crystallisation age. Although the studied grain shows a limited amount of altered domains in BSE imaging, nanoscale analyses reveal a more pervasive re-equilibration of the minerals through the percolation of fluids along dislocations.

1. Introduction

The interaction between fluids and rocks within crustal lithologies (i.e., fluid–rock interactions) represents a fundamental aspect of the geological processes of mineral transformation. Fluid-assisted mineral alteration reactions include processes such as dissolution, precipitation, and recrystallization, to which each rock constituent responds distinctively (Putnis, 2002). These processes have the potential to partially or entirely reset mineral-specific parent-daughter isotopic pairs, thereby providing the opportunity to determine the timing of fluid events in the crust (e.g., Villa and Williams, 2013). Although the mechanistic processes occurring at the fluid-mineral interface and the behaviour of U-Th-Pb during fluid alteration have been studied in detail (Seydoux-Guillaume et al., 2002a; Williams et al., 2011; Didier et al.,

* Corresponding author at: School of Earth and Planetary Sciences, Curtin University, Perth, Australia.
E-mail address: cilva.joseph@postgrad.curtin.edu.au (C. Joseph).

https://doi.org/10.1016/j.chemgeo.2023.121444
Received 6 December 2022; Received in revised form 15 March 2023; Accepted 27 March 2023
Available online 1 April 2023

2013), the longer range effect of fluid alteration beyond the recrystallisation front has not received a lot of attention. It is assumed that apparently unaltered grain domains are not affected by fluid alteration; however, it was suggested that elements could diffuse further that dissolution-reprecipitation recrystallisation fronts (Lenting et al., 2018; Geisler et al., 2019) and that fluids can percolate along dislocation networks (Tacchetto et al., 2021, 2022b). The effects of these processes at scales spanning tens of micrometres from the recrystallisation front on the U—Pb geochronometers remain untested.

Phosphate minerals are particularly reactive to fluid alteration, and their geochemical behaviour is relatively well understood from experimental and nanoscale studies (Turuani et al., 2022; Grand'Homme et al., 2016; Harlov et al., 2005, 2011). For example, experimental studies have shown that monazite undergoes partial to complete resetting of the U—Pb chronometer during alteration at 450 °C (Williams et al., 2011; Budzyń et al., 2015; Grand'Homme et al., 2016). Similarly, apatite is also highly susceptible to fluid-induced chemical and textural changes that may reset isotope systematics, thereby enabling the dating of fluid-rock interactions from the deep crust to the near-surface (Harlov, 2015; Kirkland et al., 2018a). In contrast, xenotime (Y,HREE)PO_4) is comparatively stable in fluid-mediated settings (Budzyń and Sláma, 2019). Experimental studies have shown that xenotime is stable in the low-temperature window (~250 °C) and resets partially at amphibolite facies conditions (550 °C and 650 °C), mostly by coupled dissolution–reprecipitation (Budzyń and Sláma, 2019, However, compared to other phosphates, the resilience of xenotime to fluid interaction is poorly understood, especially in low-temperature settings.

Xenotime is a common accessory mineral found in a range of rock types, including felsic intrusive rocks (Amli, 1975; Schaltegger et al., 2005; Li et al., 2013), metasedimentary metamorphic rocks (Rasmussen et al., 2011), Sn—W, gold, base metal, iron, and uranium hydrothermal deposits (Rasmussen et al., 2009, 2016; Aleinikoff et al., 2012), and sedimentary rocks, as either a detrital phase or diagenetic overgrowths on zircon (McNaughton et al., 1999; Rasmussen, 2005). The high actinide concentration, low common Pb incorporation during the growth, high closure temperature, and resistance to radiation damage make xenotime an ideal geochronometer for these geological settings (Fletcher et al., 2004; Rasmussen, 2005). Mineral-fluid interaction processes operating at the nanoscale, however, can affect the parent-daughter isotopic pair of a mineral at the scale of common geochronological techniques. In this study, we investigate the low-temperature, fluid-present alteration behaviour of xenotime, including the effects of alteration in apparently unaltered domains, using sensitive high-resolution ion microprobe (SHRIMP), transmission electron microscopy (TEM), and atom probe tomography (APT).

2. Sample and geological background

Xenotime sample z6413 (also referred to as XENO-1) comes from a granitic pegmatite from the Mesoproterozoic Grenville province of Ontario, Canada (Stern and Rayner, 2003) (Fig. 1). This sample is commonly used as a reference material for U—Pb analyses of high-U xenotime (Fletcher et al., 2004). The pegmatite is located in the ~1.6 to 1.0 Ga Central Gneiss belt (CGB) of the Grenville province, an area that dominantly comprises upper amphibolite to granulite facies orthogneiss and supracrustal units. Structurally, the Central Gneiss Belt underlies the Composite Arc Belt and overlies the Allochthon Boundary Thrust (ABT) (Ketchum and Davidson, 2000; Rivers et al., 2012). These rocks were involved in two orogenic phases. The protracted metamorphism of the Ottavan phase at ~1090–1040 Ma and the thrusting and metamorphism Rigolet phase (1020–980 Ma) (Timmermann et al., 1997; Slagstad et al., 2004; Culshaw et al., 2016). After the Grenville orogeny, no significant high-temperature metamorphic event has been reported to affect the region since the 1.0 Ga Grenville orogeny (Carr et al., 2000; Stott et al., 1991). At c. 590 Ma, the emplacement of mafic dyke swarms is associated with the opening of the Iapetus ocean and the breakup of Rodinia (Kamo et al., 1995; Spencer et al., 2015).

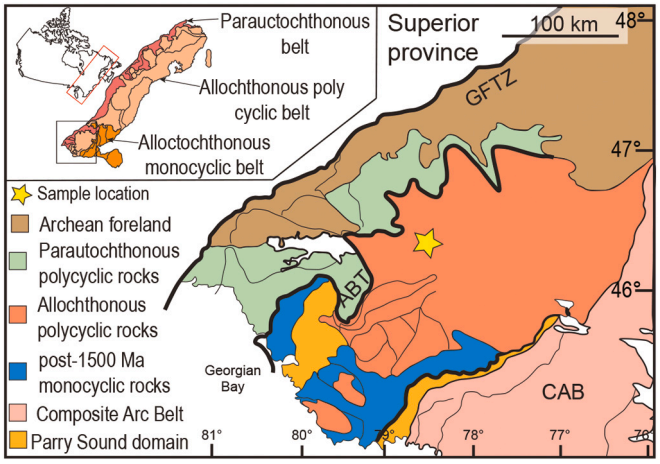

Fig. 1. Lithotectonic map of the Central Gneiss Belt, Grenville province, Ontario.
The location of the sample studied is indicated with a star symbol. Inset showing first-order subdivisions of Grenville province in Canada. GFTZ – Grenville Front Tectonic Zone, ABT – Allocthon Boundary Thrust, CAB – Composite Arc Belt. Modified from Culshaw et al., 2016; Van De Kerckhove, 2016.

Original isotope dilution thermal ionisation mass spectrometry (ID-TIMS) from xenotime z6413 yielded $^{207}Pb^*/^{206}Pb^*$ and $^{206}Pb^*/^{238}U$ ages of 996.7 ± 0.8 Ma and 993.8 ± 0.7 Ma, respectively (Stern and Rayner, 2003). Reassessing the U decay constants, Schoene et al. (2006) re-analysed z6413 and obtained slightly older $^{207}Pb^*/^{206}Pb^*$ and $^{206}Pb^*/^{238}U$ ages of 999.7 ± 0.3 Ma and 997.9 ± 0.3 Ma, respectively.

3. Methods

3.1. Scanning electron microscopy

Secondary electron (SE) and backscattered electron (BSE) images were collected using a TESCAN MIRA3 field emission scanning electron microscope (FEG-SEM) at the Microscopy and Microanalysis Facility, Curtin University.

3.2. Sensitive high-resolution ion micro-probe (SHRIMP)

U-Th-Pb analyses were conducted in two sessions on a SHRIMP II at the John de Laeter Centre, Curtin University. MG-1 was selected as the primary standard (Fletcher et al., 2004). The primary O_2^- ion beam diameter was put through a ~ 30 μm Kohler aperture to produce elliptical spots of ~10 × 7 μm with a beam current of ~0.2–0.3 nA. Six scans of the mass spectrum were recorded for each analysis, using a 9-peak run table comprising $^{194}Y_2O^+$, $^{204}Pb^+$, background ($^{204}Pb^+$ + 0.0145 AMU offset), $^{206}Pb^+$, $^{207}Pb^+$, $^{208}Pb^+$, $^{238}U^+$, $^{248}ThO^+$ and $^{254}UO^+$ (Fletcher et al., 2004). A retardation lens in front of the secondary ion collector was active to maximize abundance sensitivity.

U—Pb ratios and absolute abundances were determined relative to the MG-1 reference xenotime [$^{206}Pb^*/^{238}U$ age = 489.9 ± 0.5 Ma; $^{207}Pb^*/^{206}Pb^*$ age = 491.8 ± 1.2 Ma; U = ~900 ppm; Th = ~ 800 ppm]. SQUID3 software was used to calibrate Pb/U and Th/U using floating robust regressions through ln ($^{206}Pb^+/^{238}U^+$) vs ln ($^{254}UO^+/^{238}U^+$) for MG-1 (Bodorkos et al., 2020). Sessions 1 and 2 yielded calibration constants of 0.0052 ± 1.1% (1σ, MSWD = 1.4, p = 0.11) and 0.0076 ± 0.9% (1σ, MSWD = 1.3, p = 0.17), respectively. Common Pb was corrected using contemporaneous Pb compositions by Stacey and Kramers (1975).

Xenotime may have a wide range of possible compositions in both actinides (e.g., U = 0–6 wt%) and rare earth elements (ΣREE = 12–22%

wt%), a correction of $^{206}Pb/^{238}U$ ratios is required to account for matrix differences between the reference material and unknowns. For ln ($^{206}Pb^{+}/^{238}U^{+}$) vs ln($^{254}UO^{+}/^{238}U^{+}$), correction coefficients of fU = 6.93%, fTh = 3.23%, fΣREE = 0.7% were used (Fletcher et al., 2004). U and Th concentrations were determined via SHRIMP, using calibrations from Fletcher et al. (2000). As the primary reference material MG-1 is not homogeneous in U and Th, a ± 500 ppm uncertainty on both elements was incorporated, as in Fletcher et al. (2004), typical of the variation on primary reference material MG-1.

The ΣREE required for the matrix correction on $^{206}Pb^{*}/^{238}U$ ratio was determined using a JEOL JXA-8530F Electron Probe Micro analyser (EPMA) housed at the Centre for Microscopy, Characterisation, and Analysis at the University of Western Australia, Western Australia. The operating conditions used were a 40° take-off angle, 25 keV beam energy, and 100 nA beam current. The electron beam diameter was set to 3 × 3 μm spot size. Drake and Weill glasses and USNM phosphates from the Smithsonian institute were used as standards for instrumental calibration. The unknown values are produced using the Probe for EPMA© software package (Probe Software®). The elements were acquired using analysing crystals LiFH for Ho lβ, Yb lα, Lu lβ, Eu lα, Tb lα, Tm lα, LiF for Er lα, Nd lα, Sm lα, Gd lα, Dy la, PETJ for U mb, Zr lα, Y lα, P kα, Ca kα, Th mα, and TAP for Si kα. For Y lα, P kα, Ca kα, Lu lβ, Eu lα, Tb lα, Tm lα, Nd lα, Sm lα, Gd lα the on-peak count times were 20 s. For Er lα, Yb lα, Ho lβ, Dy lα on-peak count times were 30 s, U mb, Th mα - 60 s, Zr lα – 80 s and Si kα – 150 s. The off-peak counting time is maintained to be the same as the on-peak time. The off-peak correction method was exponential for Ca kα and U mβ, slope for Tb lα, and linear for all other elements. Unknown and standard intensities were corrected for dead time, and the latter were corrected for standard drift over time. Oxygen was calculated by cation stoichiometry and included in the matrix correction (Donovan et al., 1993). The Phi-Rho-Z algorithm utilized was Armstrong/Love Scott (Armstrong, 1988). The uncertainties on U, Th, and ΣREE are propagated in quadrature to the measured internal error on $^{206}Pb^{*}/^{238}U$.

3.3. Focused ion beam (FIB)

Samples for APT and TEM were prepared using a TESCAN Lyra3 Ga^{+} focused ion beam coupled with a scanning electron microscope (FIB-SEM) at the John the Laeter Centre, Curtin University. Both APT specimens and TEM lamellae were prepared by using the Ga^{+} ion beam operated at 30 kV accelerating voltage. Final polishing was done with a 2 kV accelerating voltage to remove the damaged layer affected by high-energy Ga^{+} ions. Seven needle-shaped APT specimens were prepared from one lift-out, and only one textural domain was targeted as described elsewhere (Rickard et al., 2020).

3.4. Transmission electron microscopy (TEM)

TEM analyses were conducted on a ≤ 100 nm thick section mounted into a copper half grid using the FEI Talos FS200X FEG TEM housed at the Microscopy and Microanalysis Facility, Curtin University. The electron beam was operated at 200 kV accelerating voltage. High-angle annular dark-field (HAADF), scanning transmission electron microscopy (STEM) images, fast Fourier transform (FFT) images, and EDS x-ray elemental maps of selected areas of the foil were collected using a double-tilted specimen holder.

3.5. Atom probe tomography (APT)

Atom probe tomography (APT) is an analytical technique that determines the distribution of major and trace elements of minerals at the sub-nanometre scale (Reddy et al., 2020). APT utilises the high field-induced evaporation of ionic species from the crystal lattice of the sample, triggered by a laser pulse applied to the apex of a needle-shaped sample. The samples used in APT are needle-shaped to meet the requirements for field evaporation and to maintain an adequate uniform field during the analysis (Gault et al., 2012). The evaporated atoms are ionised and accelerated towards the position-sensitive detector, which records the time between the laser pulse and the collision with the detector yielding time-of-flight mass spectrometry. The resultant data are in the form of a mass-to-charge spectrum and a 3D point cloud of the detected ionic species. The peaks in the mass spectrum are identified by the mass, charge state (1+ to 3+), and relative isotopic abundances of the species. For reconstruction, the lateral coordinates (x, y) of the species are obtained from the impact location on the detector and the depth (z) is determined from the sequence of evaporation of atoms.

Seven needle-shaped specimens from sample z6413 were analysed at the Geoscience Atom Probe Facility, Curtin University. The instrument (CAMECA LEAP 4000× HR) was operated in laser-assisted mode using a UV laser (λ = 355 nm). Temperature and detection rate was kept constant at 60 K and 1%, respectively, for every analysis. The laser pulse frequency was maintained at 125 kHz except for one specimen (z6413 – M2), which ran at a pulse frequency of 200 kHz. The laser pulse energy changed from 200 to 450 pJ with different analyses. The mass-to-charge spectrum was reconstructed to 3D data using the AP suite 6 software. Peaks that have intensities twice as high as background were identified and included in the 3D reconstruction. For the 3D reconstruction, voltage-based models were applied. The detector efficiency was set at 36%, k-factor at 3.3, image compression factor at 1.65, atomic volume computed at 0.01190 nm^3/atom for xenotime, and the field evaporation estimated at 28.98 V/nm as determined empirically (Fougerouse et al., 2021c).

The maximum separation method (MSM; Williams et al., 2013) was used to identify clusters in the 3D reconstructions with the following parameters: d_{max} (maximum cluster ion separation) – 1.5 nm, O (order) – 1, N (number of chemical species) – 30, L (cluster detection envelope parameter) and E (cluster detection erosion distance) both – 0.75 nm. Proximity histogram analysis was performed to determine the composition of linear features based on a 0.4 at. % Ca isoconcentration surface (above a limit of Ca concentration of 0.4 at. %) (Hellman et al., 2000) (Fig. 6).

The isotopic composition of U and Pb is measured from a narrow 0.1 Da (Dalton) range on the $^{206}Pb^{++}$ and $^{238}UO_2^{++}$ peaks and corrected for background. The background was estimated using a peak-free region (1 Da) adjacent to each peak (constant background estimation method, Joseph et al., 2021). Only U—Pb systematics were considered in this study because of the interference of the major ThO^{++} molecule with $TmPO_3^{++}$. For U – Pb systematics, the $^{206}Pb/^{238}U$ ratio is calculated using the fractionation correction method between the ratio of UO_2^{++}/UO^{++} and $^{206}Pb^{++}/^{238}UO_2^{++}$ for each analysis (Joseph et al., 2021). $^{206}Pb/^{238}U$ dates were calculated from the whole specimen and the matrix (whole specimen without clusters) using the molecular fractionation correction method (Joseph et al., 2021).

4. Results

4.1. Scanning electron microscopy

BSE imaging of the grain showed variations in grey scale density throughout the grain with a mottled appearance. Throughout the grain, thin (<1 μm) and discontinuous (10–20 μm in length), planar features can be observed on the grain surface, with a higher density of features in the central portion of the grain (Fig. 2a,b). These planar features have a preferred orientation, extending parallel to the long axis of the grain. Sub-micrometer porosity is associated with these features. Domains defined by sharp curviplanar boundaries are characterised by a dark BSE signal that can be observed trending subparallel to the long axis of the grain (Fig. 2a,c). The BSE dark domains are seen chiefly associated with the edges of the grain, although they are also present closer to the centre of the grain (Fig. 2a). The BSE dark domains are often associated with larger pores (~ 2–3 μm) compared to the minute pores (< 1 μm) in other

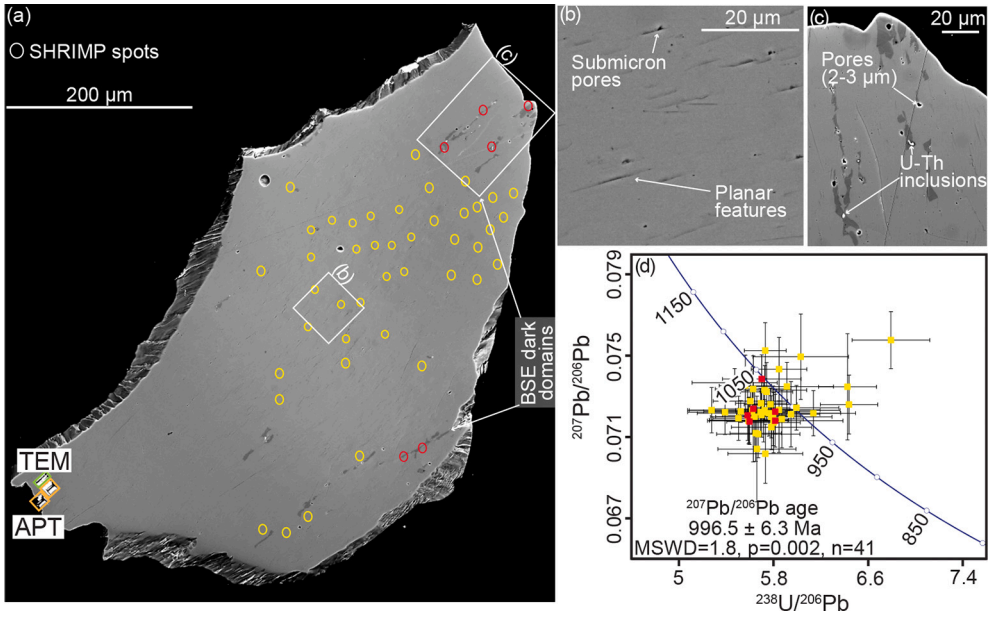

Fig. 2. a) Backscattered electron (BSE) image of grain z6413 showing altered and unaltered regions in xenotime. SHRIMP, TEM and APT sample locations are shown in the sample. SHRIMP spots colour code: yellow - unaltered region, Red - dark altered domains b) The grain shows altered mottled texture with planar features and submicron porosity. c) Showing BSE dark domains of altered xenotime, mostly seen in the outer portions of the grain with U—Th rich inclusions precipitated in the boundary of altered and unaltered domains and larger pores (2–3 μm). d) Terra-Wasserburg diagram SHRIMP results with weighted mean ^{207}Pb/^{206}Pb age. The error bars are 2σ, with the point matches to the colour-coded of grain textural domains. (For interpretation of the references to colour in this figure legend, the reader is referred to the web version of this article.)

areas of the grain. Small (~ 1–2 μm) Th—U rich inclusions are associated with the BSE dark domains. The SHRIMP analyses targeted both textural domains. The TEM and APT samples were prepared from a domain of grain devoid of BSE dark domains, and a low density of planar features in order to test the presence of alteration features away from the BSE dark domains.

4.2. Sensitive high-resolution ion micro-probe

SHRIMP analyses from the mottled zone with planar features with an average U and Th concentration of ~13,800 ppm and ~ 2400 ppm respectively, with a Th/U ratio of ~0.18 to 0.19 (Supplementary Table 1, Fig. S1a). The spot analyses targeting the BSE dark domains represent a mixture of BSE dark and mottled texture xenotime as the size of SHRIMP pits is larger than the BSE dark domains. These spots have significantly lower U and Th concentrations of ~10,870 ppm and 2030 ppm, respectively, and slightly higher and more variable Th/U ratios of ~0.18–0.22 than the rest of the grain. Regardless of the texture, common ^{204}Pb signal was below detection limit in the majority of the SHRIMP analyses. The lower concentrations of actinides with decreasing brightness in BSE are consistent with U and Th content, at least partially controlling the BSE signal.

Despite the textural variation in z6413, there does not appear to be a clear link to geochronological results. From 47 analyses, six are discordant, and they are obtained from the mottled domain. The concordant analyses from mottled ($n = 35$) and mixed mottled–BSE dark regions ($n = 6$) yield weighted mean ^{207}Pb*/^{206}Pb* ages of 996.6 ± 6.7 Ma (all 2σ, MSWD = 1.8, $p = 0.002$ [slightly over dispersed]), 996 ± 25 Ma (MSWD = 1.7, $p = 0.12$) respectively (Fig. 2d; Supplementary Table 1). Note that most analyses are slightly reversely discordant, with apparently older ^{206}Pb*/^{238}U dates. Such discrepancies are a function of using a linear correction to adjust the matrix mismatch between reference material MG-1 and z6413 (with significantly different actinide concentrations), a correction that in reality, is non-linear but difficult to model (see Fletcher et al., 2004 and Cross and Williams, 2018 for discussion). A combined weighted mean ^{207}Pb*/^{206}Pb* age of 996.5 ± 6.3 Ma (MSWD = 1.8, p = 0.002) is slightly over-dispersed but within error of the published ID-TIMS analyses (Stern and Rayner, 2003; Schoene et al., 2006). The slight over dispersion implies that there may be cryptic mobility of Pb, but this is not correlated with textures.

4.3. Transmission electron microscopy

TEM lamellae from the sample z6413 appeared mostly homogenous at low magnification. The high-angle annular dark field (HAADF) images from TEM shows the atomic number contrast in the sample, in which atoms with high atomic number will appear bright. HAADF images generated from the sample showed different grey contrasts with dark spots and bright spherical domains, ~10 nm in size (Fig. 3a). The STEM-EDS data indicate that the bright domains show enrichment in Ca and Pb, and depleted in Y, P, and O compared to the surrounding xenotime (Fig. 3c and d). High-resolution images show the mottled appearance of the xenotime host. The diffraction data from these images show the crystalline order of the sample analysed is consistent with the xenotime crystal structure. Diffraction data collected from the region of interest with bright spherical domains showed xenotime diffraction patterns along with distinctive ring patterns (Fig. 3b).

4.4. Atom probe tomography

The APT mass spectra of z6413 are consistent with the analysis of xenotime reference materials (Joseph et al., 2021) (Fig. S2a). Mass peaks up to 300 Da are obtained in which the major elements (Y, P) is present in elemental forms in various charge states and oxygen in elemental (O^+) and molecular form (O_2^+). These major Y, P, and O elements can combine to form oxides and P-bearing molecules that are evaporated in different charge states. Peaks for the rare earth elements are present as REE^+ and REE^{++} and as molecular REEO and $REEPO_3$ species. Uranium (^{238}U) was present in five peaks $^{238}UO_2^{++}$ (135.02 Da), $^{238}UO^{++}$ (127.02 Da), $^{238}UO^{+++}$ (84.68 Da), $^{238}UO_2^{+}$ (270.04 Da), and $^{238}UO_3^{+}$ (286.035 Da) (Fig. S2). No peaks in the mass spectra could be attributed to ^{235}U. ^{206}Pb and ^{207}Pb were present as doubly charged and singly charged species, with the double-charged species more dominant. No ^{204}Pb was detected above the background. The $ThPO_3^{+++}$ (103.7 Da) peak, which is close to the $^{207}Pb^{++}$ (103.49 Da) peak, was prominent and could not be deconvolved from the $^{207}Pb^{++}$ peak (Fig. S2b). Therefore, ^{207}Pb/^{206}Pb ratios were not determined for this sample.

The total amount of Ca, Pb, and U within all APT specimens is ~0.01 at. %, ~0.04 at. % and ~ 0.22 at. %, respectively. However, these elements are not homogeneously distributed. The presence of spherical and linear features enriched in trace elements was identified. Numerous Ca-Pb-rich clusters (Fig. 4a) were found, except in one specimen (M2)

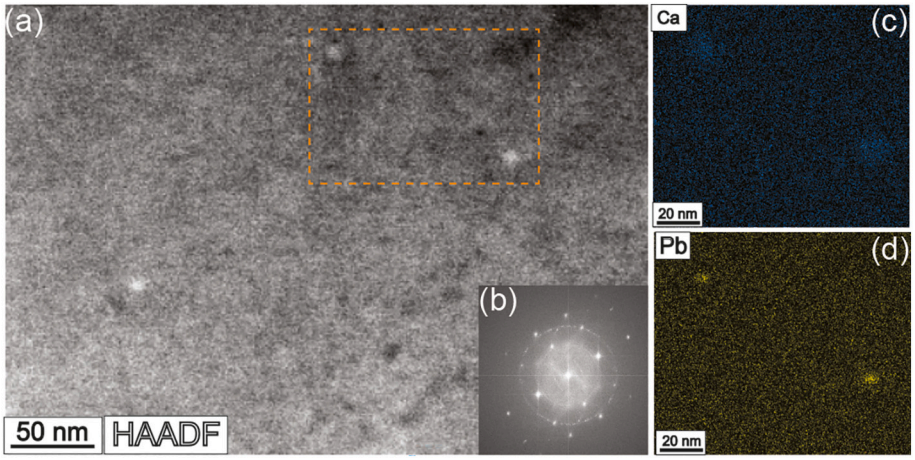

Fig. 3. a) High Angle Annular Dark Field (HAADF) image of sample z6413 showing bright spherical domains distributed in the xenotime matrix. The location of c and d is indicated with a dashed orange area; b) Diffraction pattern obtained from the same region in higher resolution (HR) mode showing circular rings along with the xenotime crystal diffraction pattern; c-d) These are EDS x-ray element maps collected with the scanning transmission electron microscope (STEM).

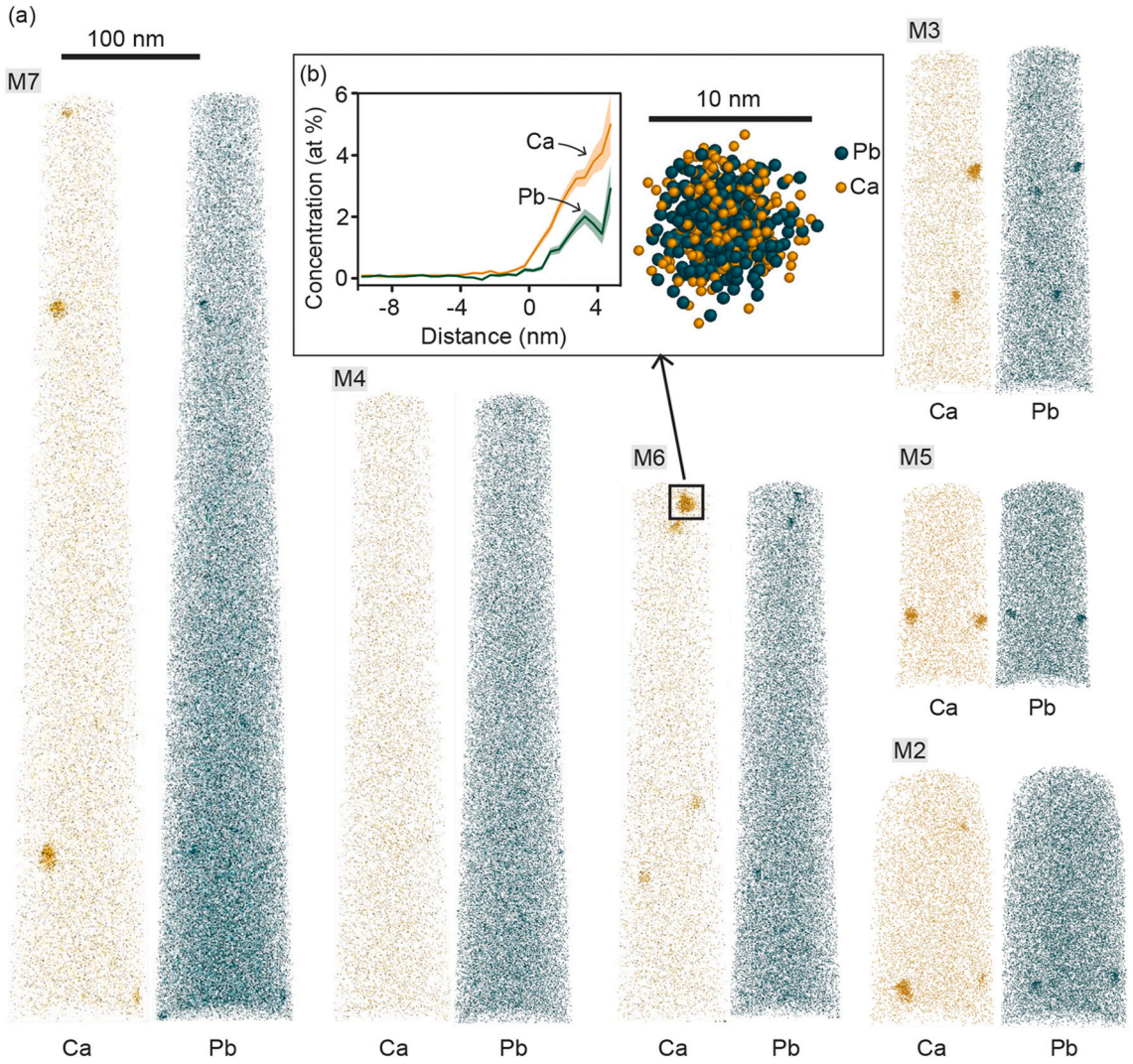

Fig. 4. a) APT 3d reconstruction of specimens from sample z6413. Each sphere represents an atom of Ca (orange) and Pb (teal). Ca-Pb* apatite inclusions are distributed heterogeneously in the xenotime matrix; b) close up of apatite inclusion and proximity histogram showing the concentration Ca and Pb in the cluster. Error 1σ. (For interpretation of the references to colour in this figure legend, the reader is referred to the web version of this article.)

where Ca and Pb were distributed homogeneously. A total of 23 clusters from the six specimens were detected. Thirteen of the 23 clusters are located on the edge of the analytical volume (partial), so their full size cannot be determined. The other ten clusters have a diameter ranging from ~4 to 18 nm (Fig. 4a). The clusters are notably enriched in Ca (up to 500× greater than in the matrix, ~ 0.01 to 5.45 at. %) and Pb (up to 70×, 0.10 to 6.70 at. %) (Fig. 4b). Other than Ca and Pb, Si was also found enriched in most of the clusters compared to the matrix (up to 5×, 0.20 to 2.36 at. %). (Fig. 4). A positive trend was observed between the size of the cluster and the Ca + Pb concentration inside the clusters (Fig. 5) and can be explained by the local magnification effect and ion trajectory aberrations during atom probe analyses (Vurpillot et al., 2000; Fougerouse et al., 2016; Reddy et al., 2020). U and Th are homogenously distributed and showed no change in concentration between the clusters and the xenotime matrix. Conversely, the clusters were depleted in Y, P, and O, the three main mineral-forming elements of xenotime, but no minor elements were significantly depleted.

In one of the APT specimens (M1), a linear feature (Fig. 6) extending at a high angle to the specimen edge is defined by enrichment of Ca (380×,~ 0.01 at. % to 2.22 at. %), Cl (210×, 0.01 at. % to 0.91 at. %), Na (65× 0.002 to 0.14 at. %), Li (8×, 0.02 at. % to 0.13 at. %), and U (4×, 0.23 at. % to 0.95 at. %) (Fig. 6b). Ca-Pb-rich clusters are also observed in the same specimen.

Using the MSM method, clusters are isolated from the whole specimen to compute U—Pb ratios. The $^{206}Pb/^{238}U$ dates of the whole specimen including the clusters, ranged from 857 ± 43 Ma to 971 ± 52 Ma with a weighted mean date of 912 ± 39 Ma (2σ; MSWD = 2.9, probability = 0.013 (Fig. 7). The matrix, excluding clusters, yielded even younger $^{206}Pb/^{238}U$ dates of 830 ± 42 Ma to 937 ± 51 Ma with a weighted mean age of 863 ± 28 Ma (2σ; MSWD = 2.1, probability = 0.047. (Supplementary Table 2) Weighted means for both the whole specimens and matrix show excess scatter for a single population (MSWD = 2.7, p = 0.014 and MSWD = 2.1, p = 0.047, respectively), indicative of nanoscale variability in age across z6413.

5. Discussion

5.1. Fluid alteration microstructures and geochronology

The grain is characterised by two textural domains, as the BSE image shows. Primarily the grain shows planar features, extending parallel to the long axis of the grain. These features are discontinuous, associated with sub-micron porosity, and widely distributed in the grain (Fig. 2b).

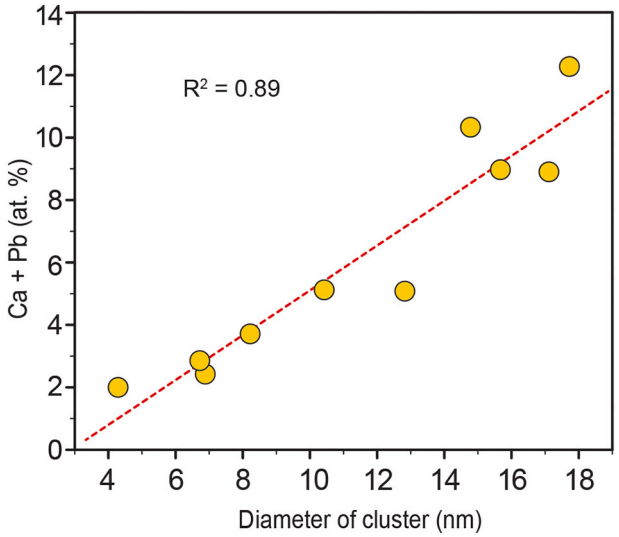

Fig. 5. Diameter of the apatite inclusions versus Ca + Pb concentration.

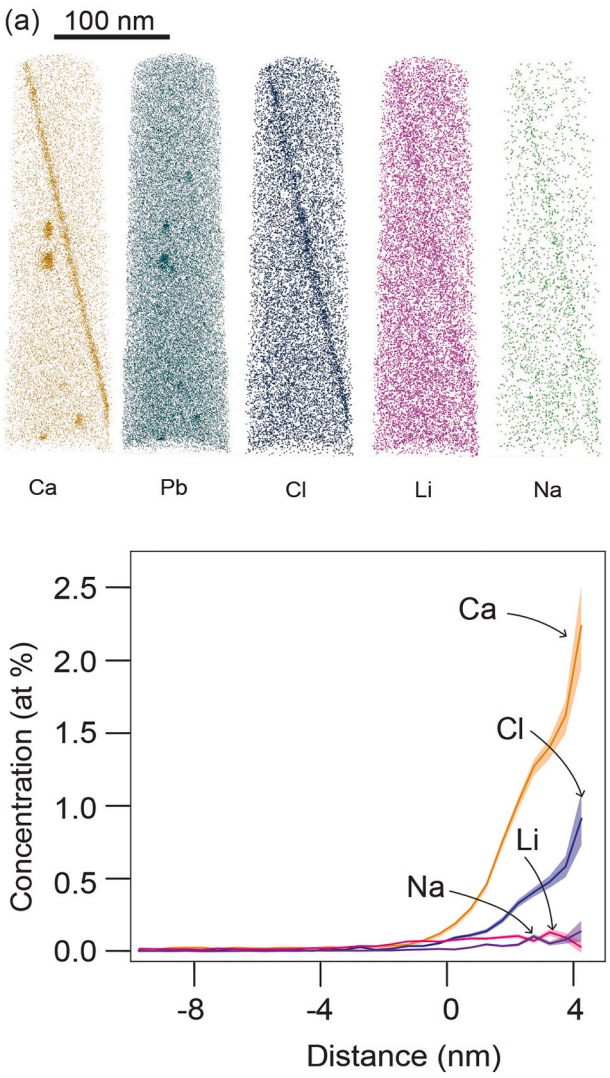

Fig. 6. a) M1 specimen showing distribution of Ca, Pb, Cl, Li, and Na in the dislocation; b) Proximity histogram of elements in the dislocation, errors are 1σ.

The planar features which have a preferred orientation, are conceived to be representing the cleavage planes of the crystal. This domain is considered unaltered based on textures and the tight range of U/Th ratio obtained from SHRIMP analyses. The dark BSE domains, coincide with a change in U and Th composition from the SHRIMP analysis. Lower actinide concentrations characterise the BSE dark domains in the grain compared to the mottled domain, which constitutes the rest of the grain. These domains have sharp boundaries with the original xenotime and are also characterised by the presence of Th-U-rich inclusions and are associated with large-scale porosity (2–3 μm; Fig. 2a,c). The depletion of U and Th from the BSE dark zones and the presence of U—Th rich inclusions are attributed to the process of fluid-assisted coupled dissolution-reprecipitation (Putnis, 2009). Based on the above observations, these BSE dark domains represent fluid-altered domains. Dissolution-reprecipitation is the process in which, in the presence of a reactive fluid, a mineral phase is replaced by an altered composition of the same phase or replaced by an entirely new phase in order to minimise Gibbs free energy (Putnis, 2002). U and Th were likely dissolved from the xenotime by the fluid and simultaneously precipitated in the form of U + Th-rich minerals such as coffinite, thorite, or uraninite in the pores, cracks, and along grain boundaries (Hetherington and Harlov, 2008; Ondrejka et al., 2016; Budzyń et al., 2018).

Results from SHRIMP analysis obtained from both altered and

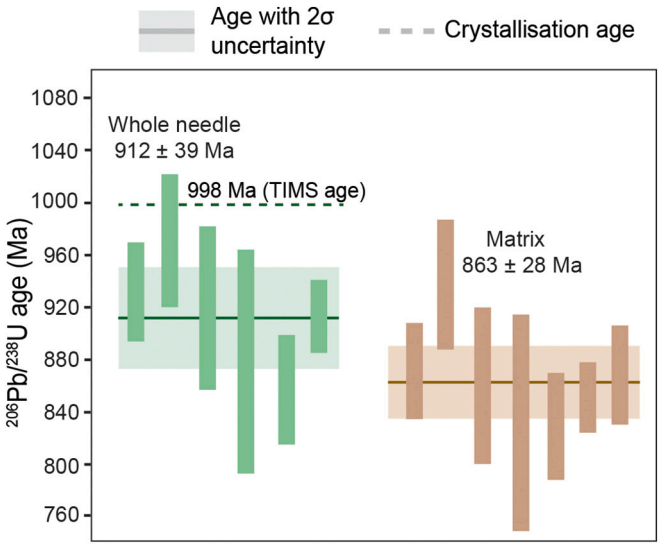

Fig. 7. APT $^{206}Pb/^{238}U$ weighted mean data of sample z6413. Green colour represents the data from whole specimen and brown represents of age of the matrix, excluding the clusters. The solid line denotes the weighted mean age obtained from the data and the dotted line represent the crystallisation age determined by TIMS. The coloured bands represents the uncertainties plotted at 2σ. (For interpretation of the references to colour in this figure legend, the reader is referred to the web version of this article.)

unaltered (mottled domain) regions of the investigated grain show no correlation of alteration with age and broadly yield the same ages as previous studies (Stern and Rayner, 2003; Rasmussen et al., 2004; Schoene et al., 2006). As a first interpretation, this suggests that the interaction of the grain with the metasomatic fluid does not affect the U—Pb system to an extent detectable by SHRIMP analysis. Alternatively, the alteration occurred in a short time after crystallisation which is not resolvable from the data. Whichever scenario is correct, it seemingly justifies the use of z6413 as reference material for U—Pb analyses. However, there is a slight excess scatter amongst concordant analyses (MSWD = 1.8, $p = 0.002$) and some discordant analyses from the unaltered domain are indicative of Pb mobility within this xenotime crystal (Fig. 2d) (Villa and Hanchar, 2017).

Xenotime is well known for its stability in an active fluid environment compared to other phosphates such as monazite and apatite (Budzyń and Kozub-Budzyń, 2015; Budzyń and Sláma, 2019; Hetherington et al., 2010). Dissolution-reprecipitation processes have been shown to partially or fully reset the U-Th-Pb isotopic systematics in high-temperature environments (Rasmussen et al., 2011; Budzyń and Sláma, 2019). However, xenotime is stable below ~450 °C in some fluid-present metamorphic and late-granitic environments (Broska et al., 2005; Janots et al., 2008; Rasmussen et al., 2011). The SHRIMP results from this study is consistent and supports the attribute of xenotime to be stable in fluid active settings. However, the data obtained from the SHRIMP is slightly over dispersed and six analyses are discordant in which the spots were from the apparently homogeneous zone of the grain.

The APT nanogeochronology results from mottled domain of the xenotime give a weighted mean $^{206}Pb/^{238}U$ date from the whole specimen 912 ± 39 Ma and the matrix 863 ± 28 Ma. The APT results suggest Pb mobility in the form of radiogenic Pb-enriched clusters and younger dates. With the exception of one specimen, all APT-determined whole specimen $^{206}Pb/^{238}U$ dates do not overlap at 2σ with the SHRIMP (996.5 ± 6.3 Ma) (Fig. 2d) and previously published ID-TIMS ages (999.7 ± 0.3 Ma) (Fig. 7). The heterogeneous distribution of Pb at the nanoscale can affect the isotopic composition measured by APT. As demonstrated in monazite, a low density of Pb clusters similar to the cluster distribution in our sample can bias nanogeochronology results (Fougerouse et al., 2018). Although the dates obtained from the whole specimen are younger than the TIMS/SHRIMP age, these younger dates are likely the results of the heterogeneous distribution of Pb clusters. Such effect is negligible in TIMS/SHRIMP data because specimen enough clusters are homogenised in the analytical volume unless Pb is diffused outside the crystal. The younger ages from the matrix, 863 ± 28 Ma compared to the crystallisation age of 999.7 ± 0.3 Ma, represents the maximum age of the event responsible for the Pb mobility into the clusters, which can also potentially lead to Pb loss out of the grain resulting in this minor discordancy. The age of 863 ± 28 Ma does not correlate with a known event in the terrain and could indicate an unidentified event or a localised event in the region.

5.2. Nanoscale compositional heterogeneities in xenotime

Based on BSE and SHRIMP results of the sample, it is established that some parts of the grain have undergone fluid alteration and present a clear example of fluid-present coupled dissolution-reprecipitation. There are numerous studies on the response of dissolution-reprecipitation reactions in minerals and also on the behaviour of the U-Th-Pb system, mainly focusing re-equilibrated grain domains and on the reaction front (Seydoux-Guillaume et al., 2002a; Williams et al., 2011; Didier et al., 2013; Ruiz-Agudo et al., 2014; Moser et al., 2022). However, whether the effect of fluids can be observed beyond the re-equilibrated domains has not received much scrutiny. In turn, the potential effect of alteration features not recognisable through petrography using classic electron microscopy techniques has not been tested.

SHRIMP analyses on the grain from this study displayed the dispersion of the Pb—Pb ages, and the discordant analyses from the apparently unaltered domain of the grain, forcing the idea that minor changes in isotopic distribution in the unaltered domain are present. The discordance is minor, but it is essential to understand these processes which are possibly operating at the nanoscale, for a better understanding of xenotime as a geochronometer and its response to fluid. Therefore this study it is aimed to analyse a region beyond the altered domains using TEM and APT, testing the long-range effect of fluid alteration.

The TEM HAADF maps showed dark patches and bright spherical domains in the grey matrix xenotime. The dark patches giving the mottled appearance are interpreted to have resulted from the annealing of radiation damage, similar to monazite and zircon (Seydoux-Guillaume et al., 2002b; Drost et al., 2013; Nasdala et al., 2020). This is explainable based on the high actinide concentration of the sample. HAADF and EDS STEM results also show bright spherical domains enriched in Ca and Pb (Fig. 3). High concentration of Pb with a higher atomic number in the spherical domains results in bright reflection signals than Y, P and O (lower atomic number than Pb) which constitutes the xenotime matrix. The diffraction data from the TEM high-resolution image shows the well-ordered xenotime structure as well as a ring pattern (Fig. 3b). The ring patterns form when electron diffraction occurs simultaneously from many different grains with different crystallographic orientations (polycrystalline nature), and as the number of crystals and randomness increase, they result in partial to complete diffraction rings (Lind, 1983). Therefore, the ring pattern indicates the presence of ultrafine (10–100 nm) polycrystalline grains with a random distribution within an otherwise ordered xenotime matrix (Asadabad and Eskandari, 2016; Lind, 1983; Asadi Asadabad and Jafari Eskandari, 2015).

Given the scale of the nanocrystalline precipitates found in TEM, it is most likely that these Ca + Pb-rich domains are the same Ca + Pb that are observed within APT specimens (Fig. 4a). Clusters in minerals have been shown to be enriched domains likely representing crystal defects (Valley et al., 2014; Peterman et al., 2016; Fougerouse et al., 2019; Verberne et al., 2020) or separate phases (Fougerouse et al., 2016, 2018, 2021b; Seydoux-Guillaume et al., 2019). In z6413, clusters have combined Ca and Pb enrichments up to 12 at. %, two to three orders of magnitude higher than the surrounding matrix. The compositional

range of the clusters is correlated with their size, with the smaller clusters comprising less Ca and Pb (Fig. 5), this compositional range is likely an analytical artefact. The analyses of multiphased materials with APT commonly suffer from local magnification effects. The local magnification effect in the atom probe analysis is due to the difference in the evaporation field for different phases (eg: precipitate vs host), which causes ion trajectory aberrations during evaporation. This leads to defocussing effects resulting in lower or higher apparent atomic density in the 3d reconstruction profile depending on the evaporation field of the analysed precipitate (Philippe et al., 2010). It has been demonstrated that due to this artefact, smaller clusters would proportionally be more affected, leading to compositional underestimation (Devaraj et al., 2014; Fougerouse et al., 2016; Reddy et al., 2020; Vurpillot et al., 2000; Tacchetto et al., 2021). Thus, all the Ca - Pb clusters observed in the studied xenotime grain might therefore represent the same mineralogical feature but with a different size distribution.

Xenotime has a tetragonal crystal structure with PO_4 tetrahedra and REO_8 (Rare earth) polyhedra, in which the RE site is occupied by Y^{3+} and $HREE^{3+}$ ions which have similar ionic radii (Y^{3+} 1.02 Å). In xenotime, Ca is incorporated into the crystal structure by $2(REE^{3+}, Y^{3+}) \leftrightarrow (Th, U)^{4+} + Ca^{2+}$ (cheralite substitution). And in the case of Pb, only a negligible amount of Pb is incorporated into the xenotime structure during its growth. Both Ca^{2+} and Pb^{2+} with ionic radii 1.29 Å and 1.12 Å, respectively are larger cations compared to the small Y^{3+} ion (1.02 Å) (Ni et al., 1995; Shannon, 1976). The Pb in the xenotime is primarily radiogenic and no signal of common Pb was detected by APT. Combining APT and TEM results from this study, it is likely these combined Ca + Pb rich are separate phases within the xenotime formed later crystallisation. Based on the composition of the clusters the phase likely to represent the mineral apatite [$Ca_5(PO_4)_3$(F, Cl, OH)] in which Pb can substitute for Ca and Si for P (Harrison et al., 2002; Pan and Fleet, 2002). Hence from here on we treat these clusters as apatite nanoscale inclusions in xenotime and the possible causes of formation are described in the next section.

One APT specimen (M1) is characterised by the presence of a linear feature primarily delineated by enrichments in Ca and Cl, but also Na, Li, Mn and U (Fig. 6). These features show similarities with fission tracks commonly observed in apatite (Donelick et al., 2005). However, xenotime has the property to rapidly self-anneal the radiation damage created by alpha recoil during radionuclide fission (Harrison et al., 2002; Rasmussen, 2005). Therefore, it is unlikely that such a feature is the result of radiation damage. Alternatively, this geometry could be representative of a linear defect of the crystal lattice (i.e., dislocation). This consideration arises from the fact that a growing number of APT studies on minerals show the local enrichment of particular elements along dislocations (Piazolo et al., 2016; Kirkland et al., 2018b; Dubosq et al., 2019; Fougerouse et al., 2019, 2021a; Schipper et al., 2020; Tacchetto et al., 2021, 2022a; Verberne et al., 2023). Within minerals, dislocations are defects produced abundantly by plastic deformation of the host crystal in response to stress (Hirth and Pond, 1996; Hull and Bacon, 2001; Barber et al., 2010). The enrichment of elements along these interfaces can include mechanisms of interface diffusion and/or segregation by defect impurity pair (Reddy et al., 2016; Verberne et al., 2022). In addition, dislocations can be formed during crystal growth in super cooled melts (Klapper, 2010; Klapper and Rudolph, 2015). Considering the above observations and the similarities with previous APT studies on mineral interfaces, the linear feature captured in the APT dataset likely represents an isolated dislocation. Unfortunately, because of the isolated character of this dislocation, its origin, deformation or growth remains unclear.

Together with Ca, the dislocation in APT specimen, M6 is enriched in exotic, fluid-mobile elements such as Cl and Na that are most notably found in saline fluids. The presence of such fluid-mobile elements along the dislocation likely represents the input from an external source. The role of dislocations as pathways for the diffusion of externally-derived trace elements has been previously described in pyrite (Fougerouse et al., 2019), titanite (Kirkland et al., 2018b), olivine (Tacchetto et al., 2021), and garnet (Tacchetto et al., 2022a). In particular, the association of Na and Cl has been attributed to the presence of a fluid infiltrating along the dislocations (Tacchetto et al., 2021). With the available dataset, we interpret the enrichment of Cl, Na, and Li to represent the signature of an externally derived fluid present during the alteration of the grain. There is a marginal increase of U in the dislocation. It is unclear whether the enrichment of U is derived from the fluid or diffused into the dislocation from the grain itself. The U^{6+} ion is highly mobile in the fluid environment. In a recent publication based on TEM observations from an unaltered zone of altered xenotime, dislocations were found to be enriched in U, Th and Si and interpreted to be responsible for age discordance (Budzyń et al., 2023). Contrary to what is expected in an apparently homogenous BSE domain, nanoscale analysis shows evidence of fluid activity in grain areas beyond the altered domains from the chemistry of the dislocation.

Therefore considering the composition of the dislocation and the sampling location of this specimen which is beyond the range of the fluid-altered domains, there is clear evidence of fluid activity inside the crystal even though it is not noticeable in textural analysis using BSE.

5.3. Formation mechanism of apatite nanoscale inclusions

Previous studies proposed different mechanisms for the formation of clusters and the mobility of Pb in minerals. For example, in zircon, a mineral that is susceptible to radiation damage, Pb-enriched clusters were formed during the thermal annealing of radiation damage during high-temperature metamorphism (Valley et al., 2014; Peterman et al., 2016, 2019, 2021). The radiation damage in zircon accumulates with time and reaches a percolation point where which the damaged sites create a network in the crystal facilitating faster diffusion of trace elements (Utsunomiya et al., 2004; Geisler et al., 2007; Pidgeon, 2014; Kusiak et al., 2015). In zircon during high temperature metamorphism, radiation damage anneals and trap Pb along with other trace elements in the damaged sites (Valley et al., 2014; Peterman et al., 2016, 2019, 2021). Similar to zircon, in rutile it is thought to be transient radiation damaged sites facilitates Pb and other trace element mobility. During high temperature metamorphism the trace elements gets trapped in the core of the damaged site of the crystal lattice which has not undergone annealing (Verberne et al., 2020). In the case of xenotime, no metamict xenotime has been observed in nature (Harrison et al., 2019). Experimental studies have proven that a phosphate phase such as xenotime have lower critical amorphisation temperature and lower activation energy for recrystallisation compared to zircon (Meldrum et al., 1997; Lenz et al., 2019; Rafiuddin et al., 2020). Xenotime recovers rapidly from radiation damage, the percolation point is never reached and Pb cannot diffuse efficiently through that process (Rasmussen, 2005; Harrison et al., 2019). In addition, the xenotime sample studied is sourced from an igneous pegmatite from a geologically stable terrain from which no significant high-temperature event ($T \sim > 300\ ^\circ C$) has been documented since the crystallisation of the pegmatite. The diffusion of Pb in xenotime is slower than other accessory minerals such as zircon and monazite and is negligible at upper crustal conditions (Cherniak, 2006, 2010). The absence of significant metamorphism also rules out the possibility for Pb volume diffusion, such that even the transient damage sites would not have attracted the impurities due to the low diffusion rates at low temperatures to form the apatite nanoscale inclusions. This feature of xenotime renders unlikely the possibility of the formation of apatite inclusions by the process of annealing of radiation damage during metamorphism, although this process cannot be excluded.

Another model to form Pb-rich clusters has been proposed for pyrite, by means of entanglement of dislocations forming energetically favourable nanoscale domains to host Pb that diffuse along dislocation cores (Fougerouse et al., 2019). The clusters observed in the data are not spatially associated with the dislocation and therefore it is unlikely that the cluster formed due to the interaction of dislocations.

Nanoscale apatite inclusions have been explained to be formed by the process of phase immiscibility, during rapid cooling in monazite from the granulite facies Sandmata complex, India (Fougerouse et al., 2018). The phase immiscibility model suggests that during rapid crystal growth excess impurities such as Ca be assimilated into the crystal structure and favours the unmixing during the cooling of the crystal (Putnis, 1992; Watson, 1996; Ferraris et al., 2005). In the APT monazite case study from the Sandmata complex, the Pb concentration in inclusions found in monazite was only up an order magnitude higher than that of the matrix (Fougerouse et al., 2018). In sample z6413, the Pb concentration in the inclusions is up to 6.7 at. % from a 0.1 at. % concentration in the matrix. The phase immiscibility model predicates that the excess Ca incorporated during rapid growth exsolved from the xenotime during cooling shortly after crystallisation. The xenotime grain studied here originated from a pegmatite (Stern and Rayner, 2003). Pegmatites crystallise at relatively low temperatures (~ 100–525 °C) and undergo relatively fast cooling (Kozłowski, 1978; Kozłowski and Marcinowska, 2007; London and Kontak, 2012; Phelps et al., 2020). Pb diffusion distance during cooling from the crystallisation temperature of the pegmatite is therefore insignificant and cannot explain up to ~7 at. % enrichment in the inclusions. Furthermore, from the nanogeochronology $^{206}Pb/^{238}U$ data of the matrix, excluding Ca-Pb-rich clusters, is 863 ± 28 Ma, which is younger than the TIMS-derived crystallisation age (Fig. 7). Therefore, the apatite nanoscale inclusions formed ~100–150 Ma after the crystallisation of the xenotime, representing a timeframe incompatible with the slow cooling model for the formation of the inclusions.

Microscale observation of xenotime grain z6413 showed fluid assisted coupled dissolution reprecipitation process which is shown as BSE dark zones, depleted in actinide concentration and concomitant precipitation of U—Th rich inclusions in the proximity of the depleted zones. This alteration is not recorded in the SHRIMP analyses from the altered domains. In nanoscale analysis, there is evidence of fluid activity based on the presence of fluid-associated elements in the dislocation. Previous studies in monazite have shown the formation of mineral inclusions due to the dissolution reprecipitation process (Harlov et al., 2011). The action of fluids provides a faster way of mass transfer with activation energy many times faster than the solid-state diffusion and it operates at low temperatures (Putnis and Austrheim, 2010). A recent study on monazite postulates that nanoscale radiogenic Pb-rich galena formed by the redistribution of radiogenic Pb during fluid dissolution-reprecipitation (Turuani et al., 2022). Our results, therefore, suggest that the apatite inclusions seen in this xenotime sample are likely be the result of a mineral-fluid reaction, 100–150 Ma after crystallisation. It is important to note that, the small field of view of nanoscale analyses limits the confidence of our interpretations and alternative models for the formation of Ca-Pb-rich nanoscale inclusions should not be discarded. However, if the clusters formed through a fluid-present alteration process, the observation of clusters in the apparently unaltered domains of the xenotime indicate that the entire grain studied here may have undergone alteration. Such features may only be observed at the nanoscale but may be pervasive at the grain scale.

5.4. Summary and geochronological implications

The xenotime grain studied in this study is affected by fluid alteration based on textural and nanoscale observations. Geochronological SHRIMP U—Pb analyses showed little or no correlation between altered and unaltered textures, indicating that the parent-daughter pair was not decoupled at the microscale, in agreement with previous studies highlighting the stability of xenotime in fluid active settings (Budzyń and Sláma, 2019). However, SHRIMP analyses recorded slight over dispersion of the data and discordant analyses which are obtained from the presumably unaltered domain. Nanoscale analyses on the unaltered domain of the sample revealed the presence of a dislocation decorated with fluid-related elements such as Cl, Na, Li, and U and apatite inclusions containing radiogenic Pb. These apatite inclusions are interpreted to form by the activity of fluid 100–150 Ma after crystallisation, pervasively throughout the studied xenotime. The fluid is responsible for radiogenic Pb redistribution at the nanoscale only and is not recorded by conventional microscale textural analyses. APT is capable of revealing fluid-rock interactions previously not recognized in microscale investigations. However, these inclusions witness a Pb mobility event that may cause minor changes in the U—Pb results from conventional analyses. The distribution of apatite inclusions in the grain could be responsible for the slight over dispersion of the SHRIMP ages. It is argued that the apatite inclusions can be the primary targets of later, more recent radiogenic Pb loss which give rise to discordant analyses. The combined micro-to-nanoscale data from this study highlights the role of apatite nanoscale inclusions to protect and retain radiogenic Pb during metasomatism. This may explain why fluid-altered xenotime geochronology yields unaffected to partially reset results, leading to the biased assumption that xenotime is more stable in fluid active settings. Instead, our results suggest that xenotime re-equilibrates extensively during metasomatism but that the U—Pb systematics are largely preserved by nanoscale heterogeneities.

Supplementary data to this article can be found online at https://doi.org/10.1016/j.chemgeo.2023.121444.

Declaration of Competing Interest

The authors declare the following financial interests/personal relationships which may be considered as potential competing interests:

Denis Fougerouse reports financial support was provided by Australian Science and Industry Endowment Fund. Denis Fougerouse reports financial support was provided by Australian Research Council.

Data availability

Data will be made available on request.

Acknowledgments

Mount 05-12 used in this project are part of the McNaughton Legacy Collection which was created by the John de Laeter Centre (JdLC). This study was supported by the Australian Science and Industry Endowment Fund (grant SIEF RI13-01) and the Discovery Early Career Research Award from the Australian Research Council to Denis Fougerouse (DE190101307). The author acknowledges the support of Microscopy and Microscopy Facility and JdLC, Curtin University whose instrumentation has been supported by University, State and Commonwealth Government funding. We are grateful for the feedback and helpful comments from the two reviewers Bernard Bingen, and Callum J. Hetherington.

References

Aleinikoff, J.N., Lack, J.F.S., Lund, K., Evans, K.V., Fanning, C.M., Mazdab, F.K., Wooden, J.L., Pillers, R.M., 2012. Constraints on the timing of Co-Cu ± Au mineralization in the Blackbird district, Idaho, using SHRIMP U-Pb ages of monazite and xenotime plus zircon ages of related Mesoproterozoic orthogneisses and metasedimentary rocks. Econ. Geol. 107, 1143–1175.

Amli, R., 1975. Mineralogy and rare Earth geochemistry of apatite and xenotime from the Gloserheia Granite Pegmatite, Froland, Southern Norway. Am. Mineral. 60, 607–620.

Armstrong, J.T., 1988. Quantitative analysis of silicates and oxide minerals comparison of Monte-Carlo, ZAF and procedures. Microbeam Anal. 239–246.

Asadabad, M.A., Eskandari, M.J., 2016. Electron diffraction. In: Kral, M.J.E.E.-M.J.E.-R. (Ed.), Modern Electron Microscopy in Physical and Life Sciences. InTech, Rijeka. Ch. 1.

Asadi Asadabad, M., Jafari Eskandari, M., 2015. Transmission electron microscopy as best technique for characterization in nanotechnology. Synth. React. Inorg. Met. Nano-Metal Chem. 45, 323–326.

Barber, D.J., Wenk, H.-R., Hirth, G., Kohlstedt, D.L., 2010. In: Hirth, J.P., L. B. T.-D, Kubin, S. (Eds.), Chapter 95 dislocations in minerals. Elsevier, pp. 171–232.

Bodorkos, S., Bowring, J.F., Rayner, N.M., 2020. Squid3: Next-Generation Data Processing Software for Sensitive High-Resolution Ion Microprobe (SHRIMP).
Broska, I., Williams, C.T., Janák, M., Nagy, G., 2005. Alteration and breakdown of xenotime-(Y) and monazite-(Ce) in granitic rocks of the Western Carpathians, Slovakia. Lithos 82, 71–83.
Budzyń, B., Kozub-Budzyń, G., 2015. The stability of xenotime in high Ca and Ca-Na systems, under experimental conditions of 250-350°C and 200-400 MPa: the implications for fluid-mediated low-temperature processes in granitic rocks. Geol. Q. 59, 316–324.
Budzyń, B., Sláma, J., 2019. Partial resetting of U–Pb ages during experimental fluid-induced re-equilibration of xenotime. Lithos 346–347, 105163.
Budzyń, B., Konečný, P., Kozub-Budzyń, G., 2015. Stability of monazite and disturbance of the Th-U-Pb system under experimental conditions of 250–350 °C and 200–400 MPa. Ann. Soc. Geol. Pol. 85.
Budzyń, B., Sláma, J., Kozub-Budzyń, G.A., Konečný, P., Holický, I., Rzepa, G., Jastrzębski, M., 2018. Constraints on the timing of multiple thermal events and re-equilibration recorded by high-U zircon and xenotime: case study of pegmatite from Piława Górna (Góry Sowie Block, SW Poland). Lithos 310–311, 65–85.
Budzyń, B., Wirth, R., Sláma, J., Kozub-Budzyń, G.A., Schreiber, A., 2023. Atomic-scale Th and U segregation into dislocation cores and U-Pb age discordance in xenotime. Lithos 107105.
Carr, S.D., Easton, R.M., Jamieson, R.A., Culshaw, N.G., 2000. Geologic transect across the Grenville orogen of Ontario and New York. Can. J. Earth Sci. 37, 193–216.
Cherniak, D.J., 2006. Pb and rare earth element diffusion in xenotime. Lithos 88, 1–14.
Cherniak, D.J., 2010. Diffusion in accessory minerals: zircon, titanite, apatite, monazite and xenotime. Rev. Mineral. Geochem. 72, 827–869.
Cross, A.J., Williams, I.S., 2018. SHRIMP U–Pb–Th xenotime (YPO4) geochronology: A novel approach for the correction of SIMS matrix effects. Chem. Geol. 484, 81–108. https://doi.org/10.1016/j.chemgeo.2017.12.017.
Culshaw, N., Foster, J., Marsh, J., Slagstad, T., Gerbi, C., 2016. Kiosk domain, Central Gneiss Belt, Grenville Province, Ontario: a labradorian palimpsest preserved in the ductile deep crust. Precambrian Res. 280, 249–278.
Devaraj, A., Colby, R., Vurpillot, F., Thevuthasan, S., 2014. Understanding atom probe tomography of oxide-supported metal nanoparticles by correlation with atomic-resolution electron microscopy and field evaporation simulation. J. Phys. Chem. Lett. 5, 1361–1367.
Didier, A., Bosse, V., Boulvais, P., Bouloton, J., Paquette, J.-L., Montel, J.-M., Devidal, J.-L., 2013. Disturbance versus preservation of U–Th–Pb ages in monazite during fluid–rock interaction: textural, chemical and isotopic in situ study in microgranites (Velay Dome, France). Contrib. Mineral. Petrol. 165, 1051–1072.
Donelick, R.A., O'Sullivan, P.B., Ketcham, R.A., 2005. Apatite fission-track analysis. Rev. Mineral. Geochem. 58, 49–94.
Donovan, J.J., Snyder, D.A., Rivers, M.L., 1993. An Improved Interference Correction for Trace Element Analysis.
Drost, K., Wirth, R., Košler, J., Fonneland Jørgensen, H., Ntaflos, T., 2013. Chemical and structural relations of epitaxial xenotime and zircon substratum in sedimentary and hydrothermal environments: a TEM study. Contrib. Mineral. Petrol. 165, 737–756.
Dubosq, R., Rogowitz, A., Schweinar, K., Gault, B., Schneider, D.A., 2019. A 2D and 3D nanostructural study of naturally deformed pyrite: assessing the links between trace element mobility and defect structures. Contrib. Mineral. Petrol. 174, 72.
Ferraris, C., White, T.J., Plévert, J., Wegner, R., 2005. Nanometric modulation in apatite. Phys. Chem. Miner. 32, 485–492.
Fletcher, I.R., Rasmussen, B., McNaughton, N.J., 2000. SHRIMP U-Pb geochronology of authigenic xenotime and its potential for dating sedimentary basins. Aust. J. Earth Sci. 47, 845–859.
Fletcher, I.R., McNaughton, N.J., Aleinikoff, J.A., Rasmussen, B., Kamo, S.L., 2004. Improved calibration procedures and new standards for U - Pb and Th - Pb dating of Phanerozoic xenotime by ion microprobe. Chem. Geol. 209, 295–314.
Fougerouse, D., Reddy, S.M., Saxey, D.W., Rickard, W.D.A., van Riessen, A., Micklethwaite, S., 2016. Nanoscale gold clusters in arsenopyrite controlled by growth rate not concentration: evidence from atom probe microscopy. Am. Mineral. 101, 1916–1919.
Fougerouse, D., Reddy, S.M., Saxey, D.W., Erickson, T.M., Kirkland, C.L., Rickard, W.D.A., Seydoux-Guillaume, A.-M., Clark, C., Buick, I.S., 2018. Nanoscale distribution of Pb in monazite revealed by atom probe microscopy. Chem. Geol. 479, 251–258.
Fougerouse, D., Reddy, S.M., Kirkland, C.L., Saxey, D.W., Rickard, W.D., Hough, R.M., 2019. Time-resolved, defect-hosted, trace element mobility in deformed Witwatersrand pyrite. Geosci. Front. 10, 55–63.
Fougerouse, D., Cavosie, A.J., Erickson, T., Reddy, S.M., Cox, M.A., Saxey, D.W., Rickard, W.D.A., Wingate, M.T.D., 2021a. A new method for dating impact events – thermal dependency on nanoscale Pb mobility in monazite shock twins. Geochim. Cosmochim. Acta 314, 381–396.
Fougerouse, D., Reddy, S.M., Seydoux-Guillaume, A.-M., Kirkland, C.L., Erickson, T.M., Saxey, D.W., Rickard, W.D.A., Jacob, D., Leroux, H., Clark, C., 2021b. Mechanical twinning of monazite expels radiogenic lead. Geology 49, 417–421.
Fougerouse, D., Saxey, D.W., Rickard, W.D.A., Reddy, S.M., Verberne, R., 2021c. Standardizing spatial reconstruction parameters for the atom probe analysis of common minerals. Microsc. Microanal. 1–10.
Gault, B., Moody, M.P., Cairney, J.M., Ringer, S.P., 2012. Atom Probe Microscopy. Springer New York, New York, NY.
Geisler, T., Schaltegger, U., Tomaschek, F., 2007. Re-equilibration of zircon in aqueous fluids and melts. Elements 3, 43–50.
Geisler, T., Dohmen, L., Lenting, C., Fritzsche, M.B.K., 2019. Real-time in situ observations of reaction and transport phenomena during silicate glass corrosion by fluid-cell Raman spectroscopy. Nat. Mater. 18, 342–348.
Grand'Homme, A., Janots, E., Seydoux-Guillaume, A.-M., Guillaume, D., Bosse, V., Magnin, V., 2016. Partial resetting of the U-Th-Pb systems in experimentally altered monazite: nanoscale evidence of incomplete replacement. Geology 44, 431–434.
Harlov, D.E., 2015. Apatite: a fingerprint for metasomatic processes. Elements 11, 171–176.
Harlov, D.E., Wirth, R., Förster, H.-J., 2005. An experimental study of dissolution–reprecipitation in fluorapatite: fluid infiltration and the formation of monazite. Contrib. Mineral. Petrol. 150, 268–286.
Harlov, D.E., Wirth, R., Hetherington, C.J., 2011. Fluid-mediated partial alteration in monazite: the role of coupled dissolution–reprecipitation in element redistribution and mass transfer. Contrib. Mineral. Petrol. 162, 329–348.
Harrison, T.M., Catlos, E.J., Montel, J.-M., 2002. U-Th-Pb dating of phosphate minerals. Rev. Mineral. Geochem. 48, 524–558.
Harrison, T.M., Catlos, E.J., Montel, J.M., 2019. U-Th-Pb dating of phosphate minerals. In: Phosphates Geochemical Geobiol. Mater. Importance, 48, pp. 523–558.
Hellman, O.C., Vandenbroucke, J.A., Rüsing, J., Isheim, D., Seidman, D.N., 2000. Analysis of three-dimensional atom-probe data by the proximity histogram. Microsc. Microanal. 6, 437–444.
Hetherington, C.J., Harlov, D.E., 2008. Metasomatic thorite and uraninite inclusions in xenotime and monazite from granitic pegmatites, Hidra anorthosite massif, southwestern Norway: mechanics and fluid chemistry. Am. Mineral. 93, 806–820.
Hetherington, C.J., Harlov, D.E., Budzyń, B., 2010. Experimental metasomatism of monazite and xenotime: mineral stability, REE mobility and fluid composition. Mineral. Petrol. 99, 165–184.
Hirth, J.P., Pond, R.C., 1996. Steps, dislocations and disconnections as interface defects relating to structure and phase transformations. Acta Mater. 44, 4749–4763.
Hull, D., Bacon, D.J., 2001. In: Hull, D., D. J. B. T.-I. to D (Eds.), 3 - Movement of Dislocations. Butterworth-Heinemann, Oxford, pp. 42–61 (Fourth E. Bacon).
Janots, E., Engi, M., Berger, A., Allaz, J., Schwarz, J.O., Spandler, C., 2008. Prograde metamorphic sequence of REE minerals in pelitic rocks of the Central Alps: implications for allanite-monazite-xenotime phase relations from 250 to 610°C. J. Metamorph. Geol. 26, 509–526.
Joseph, C., Fougerouse, D., Saxey, D.W., Verberne, R., Reddy, S.M., Rickard, W.D.A., 2021. Xenotime at the nanoscale: U-Pb geochronology and optimisation of analyses by atom probe tomography. Geostand. Geoanal. Res. 45, 443–456.
Kamo, S.L., Krogh, T.E., Kumarapeli, P.S., 1995. Age of the Grenville dyke swarm, Ontario - Quebec: implications for the timing of Iapetan rifting. Can. J. Earth Sci. 32, 273–280.
Ketchum, J.W.F., Davidson, A., 2000. Crustal architecture and tectonic assembly of the Central Gneiss Belt, southwestern Grenville Province, Canada: a new interpretation. Can. J. Earth Sci. 37, 217–234.
Kirkland, C.L., Fougerouse, D., Reddy, S.M., Hollis, J., Saxey, D.W., 2018a. Assessing the mechanisms of common Pb incorporation into titanite. Chem. Geol. 483, 558–566.
Kirkland, C.L., Yakymchuk, C., Szilas, K., Evans, N., Hollis, J., McDonald, B., Gardiner, N. J., 2018b. Apatite: a U-Pb thermochronometer or geochronometer? Lithos 318–319, 143–157.
Klapper, H., 2010. Generation and propagation of defects during crystal growth. In: Dhanaraj, G., Byrappa, K., Prasad, V., Dudley, M. (Eds.), Springer Handbook of Crystal Growth. Springer Berlin Heidelberg, Berlin, Heidelberg, pp. 93–132.
Klapper, H., Rudolph, P., 2015. Defect generation and interaction during crystal growth. In: Handbook of Crystal Growth. Elsevier, pp. 1093–1141.
Kozłowski, A., 1978. Pneumatolytic and hydrothermal activity in the Karkonosze-Izera block. Acta Geol. Pol. 28, 171–222.
Kozłowski, A., Marcinowska, A., 2007. Hydrothermal activity in the Karkonosze, Strzegom and Strzelin massifs–a fluid inclusion study. In: Granitoids Poland. AM Monogr., 1, pp. 243–252.
Kusiak, M.A., Dunkley, D.J., Wirth, R., Whitehouse, M.J., Wilde, S.A., Marquardt, K., 2015. Metallic lead nanospheres discovered in ancient zircons. Proc. Natl. Acad. Sci. 112, 4958–4963.
Lenting, C., Plümper, O., Kilburn, M., Guagliardo, P., Klinkenberg, M., Geisler, T., 2018. Towards a unifying mechanistic model for silicate glass corrosion. NPJ Mater. Degrad. 2, 28.
Lenz, C., Thorogood, G., Aughterson, R., Ionescu, M., Gregg, D.J., Davis, J., Lumpkin, G. R., 2019. The quantification of radiation damage in orthophosphates using confocal μ-luminescence spectroscopy of Nd3+. Front. Chem. 7, 1–13.
Li, Q.L., Li, X.H., Lan, Z.W., Guo, C.L., Yang, Y.N., Liu, Y., Tang, G.Q., 2013. Monazite and xenotime U-Th-Pb geochronology by ion microprobe: dating highly fractionated granites at Xihuashan tungsten mine, SE China. Contrib. Mineral. Petrol. 166, 65–80.
Lind, C.J., 1983. Characterization of Mineral Precipitates by Electron Microscope Photographs and Electron Diffraction Patterns.
London, D., Kontak, D.J., 2012. Granitic pegmatites: scientific wonders and economic bonanzas. Elements 8, 257–261.
McNaughton, N.J., Rasmussen, B., Fletcher, I.R., 1999. SHRIMP uranium-lead dating of diagenetic xenotime in siliciclastic sedimentary rocks. Science 285 (80), 78–80.
Meldrum, A., Boatner, L.A., Ewing, R.C., 1997. Displacive radiation effects in the monazite- and zircon-structure orthophosphates. Phys. Rev. B 56, 13805–13814.
Moser, A.C., Hacker, B.R., Gehrels, G.E., Seward, G.G.E., Kylander-Clark, A.R.C., Garber, J.M., 2022. Linking titanite U–Pb dates to coupled deformation and dissolution–reprecipitation. Contrib. Mineral. Petrol. 177, 42.
Nasdala, L., Akhmadaliev, S., Burakov, B.E., Chanmuang, N.C., Škoda, R., 2020. The absence of metamictisation in natural monazite. Sci. Rep. 10, 14676.
Ni, Y., Hughes, J.M., Mariano, A.N., Et, N.I., Crystal, A.L., 1995. Crystal chemistry of the monazite and xenotime structures tetrahedra and RE polyhedra, with a REOg polyhedron in xenotime that accommodates the heavy lanthanides (Tb-Lu in the synthetic phases) and a RE09 polyhedron in monazite that preferentially inco, 80, pp. 21–26.

Ondrejka, M., Putiš, M., Uher, P., Schmiedt, I., Pukančík, L., Konečný, P., 2016. Fluid-driven destabilization of REE-bearing accessory minerals in the granitic orthogneisses of North Veporic basement (Western Carpathians, Slovakia). Mineral. Petrol. 110, 561–580.
Pan, Y., Fleet, M.E., 2002. Compositions of the apatite-group minerals: substitution mechanisms and controlling factors. Rev. Mineral. Geochem. 48, 13–49.
Peterman, E.M., Reddy, S.M., Saxey, D.W., Snoeyenbos, D.R., Rickard, W.D.A., Fougerouse, D., Kylander-Clark, A.R.C., 2016. Nanogeochronology of discordant zircon measured by atom probe microscopy of Pb-enriched dislocation loops. Sci. Adv. 2.
Peterman, E.M., Reddy, S.M., Saxey, D.W., Fougerouse, D., Snoeyenbos, D.R., Rickard, W.D.A., 2019. Nanoscale processes of trace element mobility in metamorphosed zircon. Contrib. Mineral. Petrol. 174.
Peterman, E.M., Reddy, S.M., Saxey, D.W., Fougerouse, D., Quadir, M.Z., Jercinovic, M. J., 2021. Trace-element segregation to dislocation loops in experimentally heated zircon. Am. Mineral. 106, 1971–1979.
Phelps, P.R., Lee, C.-T.A., Morton, D.M., 2020. Episodes of fast crystal growth in pegmatites. Nat. Commun. 11, 4986.
Philippe, T., Gruber, M., Vurpillot, F., Blavette, D., 2010. Clustering and local magnification effects in atom probe tomography: a statistical approach. Microsc. Microanal. 16, 643–648.
Piazolo, S., La Fontaine, A., Trimby, P., Harley, S., Yang, L., Armstrong, R., Cairney, J.M., 2016. Deformation-induced trace element redistribution in zircon revealed using atom probe tomography. Nat. Commun. 7, 1–7.
Pidgeon, R.T., 2014. Zircon radiation damage ages. Chem. Geol. 367, 13–22.
Putnis, A., 1992. An Introduction to Mineral Sciences. Cambridge University Press.
Putnis, A., 2002. Mineral replacement reactions: from macroscopic observations to microscopic mechanisms. Mineral. Mag. 66, 689–708.
Putnis, A., 2009. Mineral replacement reactions. Rev. Mineral. Geochem. 70, 87–124.
Putnis, A., Austrheim, H., 2010. Fluid-induced processes: metasomatism and metamorphism. Geofluids 10, 254–269.
Rafiuddin, M.R., Seydoux-Guillaume, A.-M., Deschanels, X., Mesbah, A., Baumier, C., Szenknect, S., Dacheux, N., 2020. An in-situ electron microscopy study of dual ion-beam irradiated xenotime-type ErPO4. J. Nucl. Mater. 539, 152265.
Rasmussen, B., 2005. Radiometric dating of sedimentary rocks: the application of diagenetic xenotime geochronology. Earth Sci. Rev. 68, 197–243.
Rasmussen, B., Fletcher, I.R., Bengtson, S., McNaughton, N.J., 2004. SHRIMP U-Pb dating of diagenetic xenotime in the stirling range formation, Western Australia: 1.8 billion year minimum age for the stirling biota. Precambrian Res. 133, 329–337.
Rasmussen, B., Mueller, A.G., Fletcher, I.R., 2009. Zirconolite and xenotime U-Pb age constraints on the emplacement of the golden mile dolerite sill and gold mineralization at the Mt charlotte mine, Eastern Goldfields Province, Yilgarn Craton, Western Australia. Contrib. Mineral. Petrol. 157, 559–572.
Rasmussen, B., Fletcher, I.R., Muhling, J.R., 2011. Response of xenotime to prograde metamorphism. Contrib. Mineral. Petrol. 162, 1259–1277.
Rasmussen, B., Zi, J.W., Sheppard, S., Krapež, B., Muhling, J.R., 2016. Multiple episodes of hematite mineralization indicated by U-Pb dating of iron-ore deposits, Marquette Range, Michigan, USA. Geology 44, 547–550.
Reddy, S.M., van Riessen, A., Saxey, D.W., Johnson, T.E., Rickard, W.D.A., Fougerouse, D., Fischer, S., Prosa, T.J., Rice, K.P., Reinhard, D.A., Chen, Y., Olson, D., 2016. Mechanisms of deformation-induced trace element migration in zircon resolved by atom probe and correlative microscopy. Geochim. Cosmochim. Acta 195, 158–170.
Reddy, S.M., Saxey, D.W., Rickard, W.D.A., Fougerouse, D., Montalvo, S.D., Verberne, R., van Riessen, A., 2020. Atom probe tomography: development and application to the geosciences. Geostand. Geoanal. Res. 44, 5–50.
Rickard, W.D.A., Reddy, S.M., Saxey, D.W., Fougerouse, D., Timms, N.E., Daly, L., Peterman, E., Cavosie, A.J., Jourdan, F., 2020. Novel applications of FIB-SEM-based ToF-SIMS in atom probe tomography workflows. Microsc. Microanal. 26, 750–757.
Rivers, T., Culshaw, N., Hynes, A., Indares, A., Jamieson, R., Martignole, J., 2012. The Grenville Orogen - a post-lithoprobe perspective. In: Tecton. Styles Canada Lithoprobe Perspect, 49, pp. 97–236.
Ruiz-Agudo, E., Putnis, C.V., Putnis, A., 2014. Coupled dissolution and precipitation at mineral–fluid interfaces. Chem. Geol. 383, 132–146.
Schaltegger, U., Pettke, T., Audétat, A., Reusser, E., Heinrich, C.A., 2005. Magmatic-to-hydrothermal crystallization in the W–Sn mineralized Mole Granite (NSW, Australia). Chem. Geol. 220, 215–235.
Schipper, C.I., Rickard, W.D.A., Reddy, S.M., Saxey, D.W., Castro, J.M., Fougerouse, D., Quadir, Z., Conway, C., Prior, D.J., Lilly, K., 2020. Volcanic SiO2-cristobalite: a natural product of chemical vapor deposition. Am. Mineral. 105, 510–524.
Schoene, B., Crowley, J.L., Condon, D.J., Schmitz, M.D., Bowring, S.A., 2006. Reassessing the uranium decay constants for geochronology using ID-TIMS U-Pb data. Geochim. Cosmochim. Acta 70, 426–445.
Seydoux-Guillaume, A.-M., Paquette, J.-L., Wiedenbeck, M., Montel, J.-M., Heinrich, W., 2002a. Experimental resetting of the U–Th–Pb systems in monazite. Chem. Geol. 191, 165–181.
Seydoux-Guillaume, A.-M., Wirth, R., Heinrich, W., Montel, J.-M., 2002b. Experimental determination of thorium partitioning between monazite and xenotime using analytical electron microscopy and X-ray diffraction rietveld analysis. Eur. J. Mineral. 14, 869–878.
Seydoux-Guillaume, A.-M., Fougerouse, D., Laurent, A.T., Gardés, E., Reddy, S.M., Saxey, D.W., 2019. Nanoscale resetting of the Th/Pb system in an isotopically-closed monazite grain: a combined atom probe and transmission electron microscopy study. Geosci. Front. 10, 65–76.
Shannon, R.D., 1976. Revised effective ionic radii and systematic studies of interatomic distances in halides and chalcogenides. Acta Crystallogr. Sect. A 32, 751–767. https://doi.org/10.1107/S0567739476001551.
Slagstad, T., Hamilton, M.A., Jamieson, R.A., Culshaw, N.G., 2004. Timing and duration of melting in the mid orogenic crust: constraints from U-Pb (SHRIMP) data, Muskoka and Shawanaga domains, Grenville Province, Ontario. Can. J. Earth Sci. 41, 1339–1365.
Spencer, C.J., Cawood, P.A., Hawkesworth, C.J., Prave, A.R., Roberts, N.M.W., Horstwood, M.S.A., Whitehouse, M.J., 2015. Generation and preservation of continental crust in the Grenville Orogeny. Geosci. Front. 6, 357–372.
Stacey, J.S., Kramers, J.D., 1975. Approximation of terrestrial lead isotope evolution by a two-stage model. Earth Planet. Sci. Lett. 26, 207–221.
Stern, R.A., Rayner, N., 2003. Ages of Several Xenotime Megacrysts by ID-TIMS: Potential Reference Materials for Ion Microprobe U-Pb Geochronology.
Stott, G.M., Sutcliffe, R.H., Thurston, P.C., Williams, H.R., 1991. The Grenville Province and the Proterozoic History of Central and Southern Ontario.
Tacchetto, T., Reddy, S.M., Saxey, D.W., Fougerouse, D., Rickard, W.D.A., Clark, C., 2021. Disorientation control on trace element segregation in fluid-affected low-angle boundaries in olivine. Contrib. Mineral. Petrol. 176, 1–16.
Tacchetto, T., Clark, C., Erickson, T., Reddy, S.M., Bhowany, K., Hand, M., 2022a. Weakening the lower crust: conditions, reactions and deformation. Lithos 422–423, 106738.
Tacchetto, T., Reddy, S.M., Fougerouse, D., Clark, C., Saxey, D.W., Rickard, W.D.A., 2022b. Crystal plasticity enhances trace element mobility in garnet. Geology 50, 1387–1392.
Timmermann, H., Jamieson, R.A., Culshaw, N.G., Parrish, R.R., 1997. Time of metamorphism beneath the Central Metasedimentary Belt boundary thrust zone, Grenville Orogen, Ontario: accretion at 1080 Ma? Can. J. Earth Sci. 34, 1023–1029.
Turuani, M.J., Laurent, A.T., Seydoux-Guillaume, A.-M., Fougerouse, D., Saxey, D., Reddy, S.M., Harley, S.L., Reynaud, S., Rickard, W.D.A., 2022. Partial retention of radiogenic Pb in galena nanocrystals explains discordance in monazite from Napier complex (Antarctica). Earth Planet. Sci. Lett. 588, 117567.
Utsunomiya, S., Palenik, C.S., Valley, J.W., Cavosie, A.J., Wilde, S.A., Ewing, R.C., 2004. Nanoscale occurrence of Pb in an Archean zircon. Geochim. Cosmochim. Acta 68, 4679–4686.
Valley, J.W., Cavosie, A.J., Ushikubo, T., Reinhard, D.A., Lawrence, D.F., Larson, D.J., Clifton, P.H., Kelly, T.F., Wilde, S.A., Moser, D.E., Spicuzza, M.J., 2014. Hadean age for a post-magma-ocean zircon confirmed by atom-probe tomography. Nat. Geosci. 7, 219–223.
Van De Kerckhove, S.R., 2016. Tectonic History of the Nepewassi Domain, Central Gneiss Belt, Grenville Province, Ontario: A Lithological, Structural, Metamorphic and Geochronological Study.
Verberne, R., Reddy, S.M., Saxey, D.W., Fougerouse, D., Rickard, W.D.A., Plavsa, D., Agangi, A., Kylander-Clark, A.R.C., 2020. The geochemical and geochronological implications of nanoscale trace-element clusters in rutile. Geology 48, 1126–1130.
Verberne, R., Reddy, S.M., Saxey, D.W., Fougerouse, D., Rickard, W.D.A., Quadir, Z., Evans, N.J., Clark, C., 2022. Dislocations in minerals: fast-diffusion pathways or trace-element traps? Earth Planet. Sci. Lett. 584, 117517.
Verberne, R., van Schrojenstein Lantman, H.W., Reddy, S.M., Alvaro, M., Wallis, D., Fougerouse, D., Langone, A., Saxey, D.W., Rickard, W.D.A., 2023. Trace-element heterogeneity in rutile linked to dislocation structures: Implications for Zr-in-rutile geothermometry. J. Metamorph. Geol. 41, 3–24. https://doi.org/10.1111/jmg.12686.
Villa, I.M., Hanchar, J.M., 2017. Age discordance and mineralogy. Am. Mineral. 102, 2422–2439.
Villa, I.M., Williams, M.L., 2013. Geochronology of metasomatic events. In: Lecture Notes in Earth System Sciences, pp. 171–202.
Vurpillot, F., Bostel, A., Blavette, D., 2000. Trajectory overlaps and local magnification in three-dimensional atom probe. Appl. Phys. Lett. 76, 3127–3129.
Watson, E.B., 1996. Surface enrichment and trace-element uptake during crystal growth. Geochim. Cosmochim. Acta 60, 5013–5020.
Williams, M.L., Jercinovic, M.J., Harlov, D.E., Budzyń, B., Hetherington, C.J., 2011. Resetting monazite ages during fluid-related alteration. Chem. Geol. 283, 218–225.
Williams, C.A., Haley, D., Marquis, E.A., Smith, G.D.W., Moody, M.P., 2013. Defining clusters in APT reconstructions of ODS steels. Ultramicroscopy 132, 271–278.